Finite-size scaling on the torus with periodic projected entangled-pair states

Gleb Fedorovich,[1,*] Lukas Devos,[1] Jutho Haegeman,[1] Laurens Vanderstraeten,[2] Frank Verstraete,[1,3] and Atsushi Ueda[1]

[1] *Department of Physics and Astronomy, Ghent University, Krijgslaan 281, 9000 Gent, Belgium*
[2] *Center for Nonlinear Phenomena and Complex Systems, Université Libre de Bruxelles, Belgium*
[3] *Department of Applied Mathematics and Theoretical Physics, University of Cambridge, Wilberforce Road, Cambridge, CB3 0WA, United Kingdom*

(Dated: April 17, 2025)

An efficient algorithm is constructed for contracting two-dimensional tensor networks under periodic boundary conditions. The central ingredient is a novel renormalization step that scales linearly with system size, i.e., from $L \to L+1$. The numerical accuracy is comparable to state-of-the-art tensor network methods, while giving access to much more data points, and at a lower computational cost. Combining this contraction routine with the use of automatic differentiation, we arrive at an efficient algorithm for optimizing fully translation invariant projected entangled-pair states on the torus. Our benchmarks show that this method yields finite-size energy results that are comparable to those from quantum Monte Carlo simulations. When combined with field-theoretical scaling techniques, our approach enables accurate estimates of critical properties for two-dimensional quantum lattice systems.

I. INTRODUCTION

Quantum many-body systems at criticality exhibit exciting emergent phenomena. The unifying picture for understanding quantum criticality is given by the renormalization group: the low-energy or long-distance properties of critical systems are described by field theories. Originally, it was assumed that these field theories are always related to fluctuations of some local order parameters that characterize the phase transition, but nowadays several instances are known of exotic quantum critical points that defy this standard picture.

In this context, the role of numerical methods is crucial for establishing whether these more exotic instances of quantum criticality can occur in microscopic models. Finite computational resources, however, can never reproduce the nonanalytic properties of an infinite system at criticality. In numerical approaches such as exact diagonalization or quantum Monte Carlo, it is the finite size of the system that leads to a regularization of the critical signatures. Fortunately, the theory of finite-size scaling was developed [1–4]: the critical properties can be determined numerically from the scaling of different quantities as the system size is increased. With the formulation of powerful scaling hypotheses, this approach has led to many successes in revealing the universal critical properties in many microscopic models, or, on the contrary, showing that certain models in fact do not obey the expected scaling properties.

Another numerical approach for studying quantum critical systems is using tensor networks as variational wavefunctions for approximating their ground states [5]. In contrast to finite-size methods, tensor networks can be formulated directly in the thermodynamic limit when some kind of translation invariance is present in the system, but they are limited in the amount of entanglement they can capture – this limitation is typically expressed as the bond dimension of the tensor network, which can be systematically increased to reach more precise results. In analogy to finite-size scaling, a theory of finite-entanglement scaling [6–9] is currently under construction to extract the critical properties of a given many-body system systematically. For one-dimensional (1-D) systems, methods based on the formalism of matrix product states (MPS) are extremely efficient for obtaining numerical results at very high bond dimensions [10], and a number of tools [11–16] are available for extracting critical properties for generic models.

In a parallel development, tensor networks have also been used to encode the ideas of the renormalization group in a more explicit sense. For a 1-D quantum system, the multiscale entanglement renormalization ansatz (MERA) [17, 18] was proposed to represent the ground states of critical models. Although this approach is less efficient than the MPS-based algorithms, the scaling properties of critical ground states are naturally represented and precise scaling dimensions were determined for some critical models [19, 20]. In the context of statistical mechanics, similar ideas have led to different real-space renormalization schemes such as the tensor renormalization group (TRG) [21–26] and tensor network renormalization (TNR) [27–30], which capture the scaling properties of critical models in two dimensions and beyond.

For two-dimensional (2-D) quantum systems, the formalism of projected entangled pair states (PEPS) [31, 32] and tree tensor networks (TTN) [33–35] can be used efficiently to represent correlated ground states. Again, PEPS can be formulated and manipulated directly for infinite system sizes [36], but extracting critical properties is less straightforward. On the one hand, the numerical methods are computationally more demanding, so

* gleb.fedorovich@ugent.be

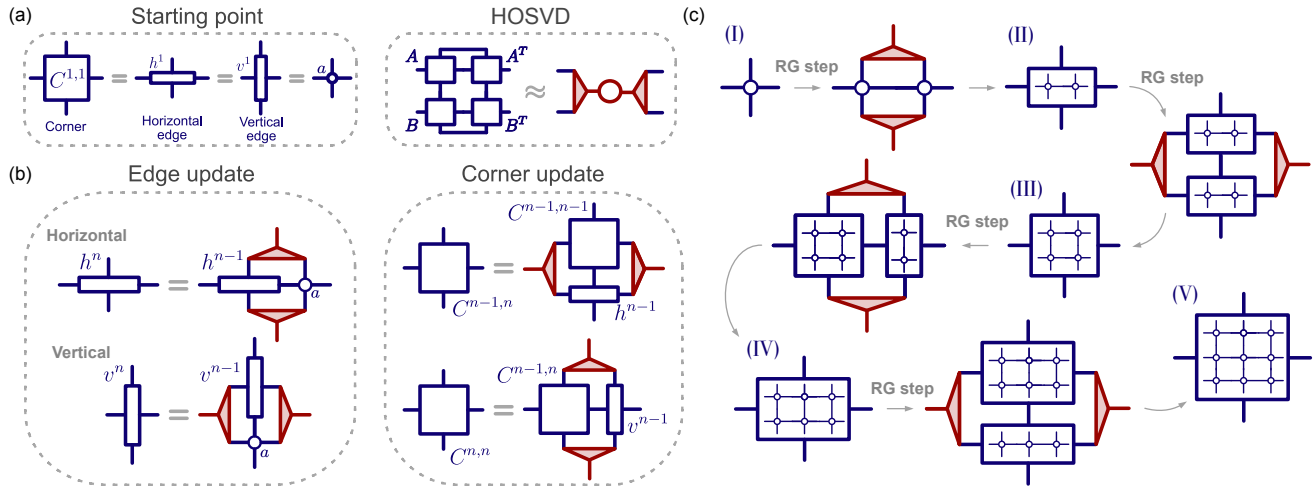

FIG. 1. Schematic illustrations of the coarse-graining procedure in PTMRG. The coarse-grained tensors consist of four types of tensors: a, h^n, v^n, and $C^{n,m}$. In the context of a PEPS simulation, a represents the inner product of the two local PEPS tensors, whereas it is the local tensor encoding the Boltzmann weights in the context of a partition function. Tensors h^n, v^n and $C^{n,m}$ respectively represent coarse-grained tensor of $n \times 1$, $1 \times m$, and $n \times m$ tensor network of a. (a) All initial tensors are set to be a. The isometries involved in RG steps are obtained via HOSVD. (b) Throughout the RG, h and v are iteratively combined with a to expand the system size by one. Similarly, C is combined with h and v when we expand the system in the vertical and horizontal directions, respectively. (c) An example of 3 by 3 PEPS tensor network contracted via PTMRG scheme that alternately coarse-grains the tensor in the vertical and horizontal direction twice.

the accessible range of bond dimensions is smaller than in the 1-D MPS case. On the other hand, the theory of finite-entanglement scaling for PEPS [37–40] is still in full development.

Given this situation, it makes sense to investigate whether the use of variational tensor network methods for performing finite-size scaling could lead to a complementary approach to studying quantum critical systems. The main objection concerns the fact that finite-size scaling is performed preferably on systems with periodic boundary conditions, which are a lot more demanding to simulate with tensor networks than systems with open boundary conditions. Nonetheless, several works [41–50] have shown that MPS can be used efficiently for periodic systems to extract critical properties. In particular, in Refs. [44, 46], it was shown that uniform MPS on a periodic system can be optimized efficiently. In Ref. [51], a periodic PEPS algorithm was constructed by using a PEPS with open boundary conditions and taking an extensive superposition of translated copies to restore the translation symmetry of the system. By using sampling techniques and stochastic optimization, this ansatz was efficiently optimized using high-performance and parallelized computing.

In this work, we introduce an algorithm for directly optimizing a single periodic PEPS wavefunction. This approach implements the translation invariance of the periodic geometry in the most natural way, thereby requiring significantly fewer variational parameters for the same accuracy. Our algorithm is based on an efficient contraction routine of periodic 2-D tensor networks, which combines ideas from the real-space renormalization ideas that have been used for simulating 2-D stat-mech models, such as TRG/TNR and the corner transfer matrix renormalization group (CTMRG) [52–55]. We then combine this contraction routine with the use of automatic differentiation (AD) to variationally optimize periodic PEPS wavefunctions.

II. CONTRACTION OF PERIODIC 2D TENSOR NETWORKS

The backbone of any PEPS algorithm is an efficient routine to accurately approximate expectation values by contracting the resulting tensor network. For infinite PEPS, boundary MPS methods [32, 56, 57] and CMTRG variants [52–55, 58–60] are the most viable options, but these cannot be readily applied in the periodic case. Real-space RG methods such as TRG and TNR can be used to efficiently contract periodic systems [61–68], but typically implement scale transformations of the lattice so that system sizes have to come in logarithmic spacings if translation invariance is to be respected after every coarse-graining step. In this work, therefore, we propose a periodic transfer matrix renormalization group (PTMRG) method, which combines ideas from the CTMRG and TRG approaches.

A. Periodic transfer matrix renormalization group (PTMRG)

The main steps of the proposed PTMRG scheme are illustrated in Fig. 1. Given a homogeneous $L \times L$ network of contracted four-leg tensors a, we first introduce a coarse-grained tensor $C^{n,m}$ and a vertical (horizontal) edge tensor v^n (h^n), where the superscripts indicate the system size associated with each tensor. In other words, $C^{n,m}$ describes a system with $n \times m$ sites in total, while v^n (h^n) represents a vertical (horizontal) n-site chain containing a tensors.

Initializing $C^{1,1} = h^1 = v^1 = a$, we develop the update rules that are presented in Fig. 1(b). More precisely, following the standard HOSVD approach [61, 69], we obtain isometries based on $C^{n-1,n-1}$ and h^{n-1} environment tensors, and perform a single horizontal sweep to get $C^{n-1,n}$ and h^n. As usual for most TRG schemes, the isometries guarantee to avoid exponentially growing bond dimension by introducing a threshold for the truncation dimension χ. In the same way we perform a vertical sweep to get $C^{n,n}$ and v^n from $C^{n-1,n}$ and v^{n-1}. By sequentially applying horizontal and vertical transformations L times, the final coarse-grained tensor $C^{L,L}$ represents the $L \times L$ system. Finally, since we are mostly interested in studying finite systems with periodic boundary conditions (on a torus), one can straightforwardly contract the top-bottom and left-right legs of the coarse-grained environment tensors.

Regarding the CPU time required to perform a single RG contraction, the proposed PTMRG scheme has a reduced scaling by using at each renormalization step a given local four-leg tensor a with fixed bond dimension D. The computational complexity of TRG and HOTRG schemes scale as $O(\chi^6)$ [21] and $O(\chi^7)$ [61] respectively, while the PTMRG algorithm scales as $O(\chi^5)$ – we refer to Appendix C for a detailed analysis of the scaling of the algorithm. We confirm this scaling behavior in the following subsection while benchmarking the evaluation of the partition function of the 2-D classical Ising model.

B. Application to 2-D statistical mechanics

To demonstrate the performance of the PTMRG contraction scheme, we consider the classical Ising model on a square lattice,

$$E_{\text{Ising}}(\{\sigma_i\}) = -\sum_{\langle ij \rangle} \sigma_i \sigma_j, \qquad \sigma_i = \pm 1 \tag{1}$$

with PBC at the critical temperature $T_c = 2/\ln(1+\sqrt{2})$. When computing the statistical model, we aim to evaluate the partition function with PBC, denoted as $Z(L, L)$. For the classical Ising model on a square lattice, this is represented by $L \times L$ contractions of the four-leg local tensor $T^{(1)}_{ijkl}$, as described in Ref. [70]:

$$T^{(1)}_{ijkl} = 2\cosh^2(\beta) f_i f_j f_k f_l \delta_{\text{mod}[i+j+k+l,2],0},$$

where β is the inverse temperature, and $f_n = \sqrt{\tanh(\beta)}^{\,n}$. The indices i, j, k, l (left, top, right, down) take values of 0 or 1. Contracting these tensors corresponds to summing over spin configurations, and performing this contraction on a $L \times L$ lattice enables us to compute the entire partition function. Specifically, we use $C^{L,L}$ from PTMRG to compute the partition function starting from the initial tensor $a = T^{(1)}_{ijkl}$.

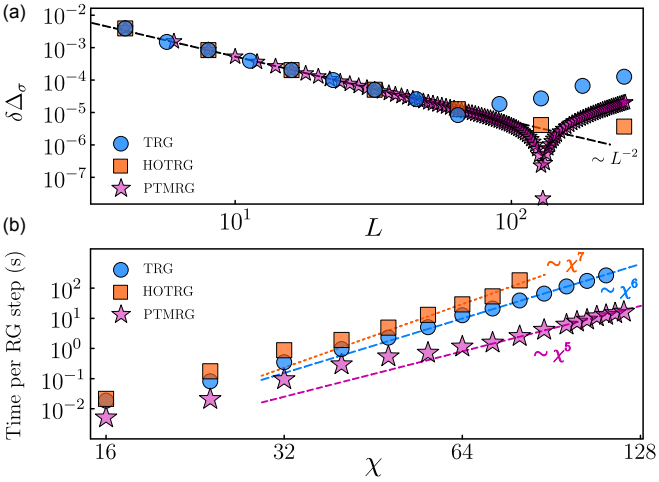

FIG. 2. (a) Finite-size effect $\delta\Delta_\sigma(L)$ computed from TRG($\chi = 64$), HOTRG($\chi = 56$), and PTMRG($\chi = 112$). The theoretical scaling $\propto 1/L^2$ is shown by a black dashed line. (b) The average computational time per RG step for the critical Ising model. The dashed lines show the expected asymptotic scalings with respect to the truncation dimension χ.

Figure 2(a) shows the computational time required to perform one update step for TRG, HOTRG, and PTMRG [1]. When using the same bond dimension χ, PTMRG is faster by one order of magnitude. Consequently, more data points can be collected in the same computational time.

In addition to its computational efficiency, PTMRG also demonstrates high accuracy. TRG/TNR algorithms are known to introduce numerical errors due to the bond dimension truncation [21, 27–29, 66, 67, 71–73], with these errors being most severe in critical systems with a diverging correlation length. This challenging scenario can be used to estimate the accuracy of the algorithm. At criticality, the transfer matrix, obtained by contracting two horizontal legs of $C^{L,L}$, has a universal spectrum

[1] We calculate the average time consumed per step after omitting the first few steps where the bond dimension is still growing to its maximal value.

Λ_n [2]. This Λ_n corresponds to the scaling dimension Δ_n of the conformal field theory (CFT) as

$$\Lambda_n = A \exp(-2\pi\Delta_n), \tag{2}$$

where the eigenvalues are ordered in descending order, and A is a nonuniversal constant [74–76]. For unitary CFTs, Δ_0 is zero, so we can obtain the scaling dimension by taking the ratios of the eigenvalues as

$$\Delta_n = \frac{1}{2\pi} \ln(\Lambda_0/\Lambda_n).$$

This universal spectrum can be used to gauge the numerical error because the deviation from the universal value is attributed to the numerical error as discussed in Ref. [72]. In particular, the deviation in the second leading eigenvalue is known to capture this effect well. We define this deviation as

$$\delta\Delta_\sigma = |\Delta_\sigma - \Delta_\sigma(L)|, \tag{3}$$

where $\Delta_\sigma(L) = \frac{1}{2\pi} \ln(\Lambda_0/\Lambda_1)$ and $\Delta_\sigma = \frac{1}{8}$ is the scaling dimension for the corresponding state. In addition to the numerical errors, Δ_σ contains a finite-size effect that decays as $\propto L^{-2}$ due to the leading irrelevant operator. Thus, the numerical error should manifest as a deviation of $\delta\Delta_\sigma$ from this $\sim L^{-2}$ line.

Figure 2(b) displays $\delta\Delta_\sigma$ obtained from TRG ($\chi = 64$), HOTRG ($\chi = 56$), and PTMRG ($\chi = 112$). We choose these bond dimensions so that the computational time per step is the same, as can be read off from (a). First, we find that the TRG data points quickly drift away from the expected finite-size scaling $\sim L^{-2}$ denoted with a dotted line around $L = 64$, allowing us to use only eight data points as reliable data. Similarly, there are only five reliable HOTRG data points up to $L = 64$ before the deviation at $L = 128$. However, the data points of PTMRG exhibit correct scaling up to $L \sim 100$ with approximately fifty data points. From this point of view, PTMRG has a significant advantage over TRG and HOTRG, allowing us to obtain more data points before truncation errors become significant. We expect this aspect to prove valuable for finite-size scaling in statistical mechanics models, providing more reliable results in TRG schemes.

III. PERIODIC PEPS ALGORITHM

Given an efficient method for contracting periodic 2-D tensor networks, we can now develop our periodic PEPS algorithm. For infinite PEPS, the original algorithms for optimizing the local tensors were based on applying imaginary time evolution via the Trotter-Suzuki decomposition to a random initial state, using varying levels of accuracy and sophistication known as simple update [77], full update [36], cluster update [78] and fast-full update [79]. More recently, progress was made using various direct energy minimization approaches based on DMRG-like optimisation [80] as well as gradient-based numerical optimization methods [81]. These more recent strategies outperform the methods based on imaginary time evolution in terms of their ability to find the optimal state at a given bond dimension. Furthermore, the gradient-based methods have become very efficient by incorporating the use of automatic differentiation (AD) [82]: given an efficient contraction routine for evaluating the variational energy, one can simply apply AD to compute the gradient [83] and optimize the variational energy.

However, all of these developments are centered around uniform PEPS in the thermodynamic limit. Optimization of finite PEPS [84, 85] has proven to be considerably more difficult, although the sampling and stochastic optimization of generic PEPS [51, 86, 87] and TEBD or DMRG like optimizations for the restricted set of isometric PEPS [88, 89] have been carried out successfully. All of these approaches are formulated for systems with open boundary conditions, where all the tensors have to be chosen differently. In the absence of a canonical form for PEPS, this makes the optimization very costly.

On the torus, the situation is very different. Because of translation invariance, we can choose a uniform PEPS parametrization in terms of a single local tensor A with bond dimension D, similar to the case of infinite PEPS. Additionally, we can impose other symmetries on the PEPS tensor such as reflection and rotation symmetries. The contraction of a periodic PEPS can be performed using the PTMRG approach of the previous section for a double-layer tensor network, whereas the evaluation of a local expectation value is performed by a single extension (see Fig. 3). The optimization problem that we want to solve is then given by

$$\epsilon_0(A) = \min_A \frac{\langle\Psi(A)|h|\Psi(A)\rangle}{\langle\Psi(A)|\Psi(A)\rangle}, \tag{4}$$

where $|\Psi(A)\rangle$ denotes the PEPS wavefunction that is generated by the tensor A, and h is a nearest-neighbour term in the hamiltonian. Note that we have to evaluate only a single term since all the other terms in the Hamiltonian are identical due to the translation or rotation symmetry of the PEPS. This optimization problem is now solved using the automatic differentiation (AD) approach.

The proposed algorithm is shown in Fig. 3 and contains the following main steps:

1: Merge the given local A-PEPS and $A^\dagger$-PEPSs into an a-tensor
2: Using the PTMRG scheme, obtain environment tensors $C^{L-1,L-2}$ as well as v^{L-1} and h^{L-1}
3: Given a two-site Hamiltonian, compute the current energy expectation value (as illustrated in the right panel of Fig. 3)
4: Using AD and the energy expectation value as a cost function, update the local PEPS tensor to get a lower

[2] To improve accuracy, we construct a 2×1 transfer matrix from $C^{L,L}$ when computing Fig. 2(a).

energy state

5: Repeat steps (1)-(4) until the desired convergence is fulfilled

In this way, the AD approach allows us to compute the gradient of the energy expectation value as a function of the local PEPS tensor and apply a gradient-based nonlinear optimization method to perform the energy minimization. Based on our experience, we find the quasi-Newton L-BFGS method [90] to be the most efficient and robust approach for this particular case.

It is worth pointing out a particular pathological problem that can occur when running a gradient-based PEPS optimization[3]. We observe that after several dozen optimization steps, the gradient of the energy sometimes starts to increase dramatically until the line search involved in finding the next optimization step fails. To the best of our knowledge, the origin of the following problem is the discontinuity of the energy function in the PEPS manifold due to truncation errors. Indeed, the energy and associated gradient that is used in the optimization are not the exact PEPS energy. While the latter can be assumed to be smooth, at least for finite systems as is the case here, it cannot be computed exactly. The approximations in evaluating the energy, in this case provided by the truncation step in the PTMRG algorithm, can result in discontinuities (because of e.g. level crossings in the singular value spectrum) and errors which are not variational in origin, *i.e.* which cause the approximated energy to be lower than the exact result. The exact gradient of this approximate energy can guide the optimization process towards exploiting these numerical errors, resulting in unreliable results, such as significantly lower energy with a relatively large gradient norm. The detailed discussion as well as an illustrative example are presented in Appendix B. Therefore, one needs to find a sweet spot for the truncation dimension χ to balance between sufficient accuracy and manageable computational cost (in both memory and runtime).

IV. BENCHMARK: TRANSVERSE FIELD ISING MODEL

As a first example, we consider the 2-D quantum transverse field Ising model (TFIM) on a square lattice represented by the following Hamiltonian:

$$\hat{H}_{\mathrm{TFIM}} = -\sum_{\langle ij\rangle} \hat{\sigma}_i^z \hat{\sigma}_j^z - \lambda \sum_i \hat{\sigma}_i^x, \quad \lambda > 0, \tag{5}$$

where σ^z, σ^x are Pauli matrices, $\langle ij\rangle$ stands for the summation over all nearest-neighbour pairs, and λ is the magnitude of the transverse field. For $\lambda = \lambda_{\mathrm{crit}} \approx 3.04438$ there is a phase transition between symmetry-broken and disordered phases in an infinite system.

[3] We have observed that the same issue can occur in AD optimization of infinite PEPS.

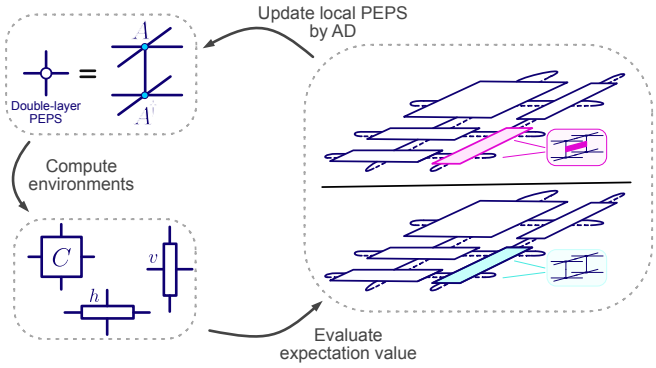

FIG. 3. Schematic picture of the periodic PEPS algorithm. We minimize the expectation value of the local Hamiltonian with respect to the local PEPS tensor, as shown in Eq. (4). The $n \times n$ contraction of a tensors is replaced by the coarse-grained tensors to maintain the numerical tractability. For the numerator of Eq. (4), two a are replaced by the two-site impurity denoted by a pink rectangular tensor. Once the evaluation is done, AD minimizes this cost function using gradient-based methods.

We perform PEPS optimization using PTMRG (see Sec. II A) and study finite-size scaling for different system sizes $L = 3, 4, 5, .., 10$ as well as local PEPS bond dimension $D = 2, 3, 4$. At the critical point, the ground state energy per site of a finite 2-D quantum system should scale as follows [91]:

$$\epsilon_0(L) \approx \epsilon_0 + \frac{\alpha}{L^3} + \dots . \tag{6}$$

This behavior is due to the nature of the low-lying energy states, which exhibit a linear dispersion (and thus Lorentz invariance) at the criticality of this model. In contrast, the gapped case leads to exponential corrections to the total energy, or thus, for the energy density [92–95]:

$$\epsilon_0(L) \approx \epsilon_0 + \frac{\bar{\alpha} e^{-L/\xi}}{L^2} + \dots . \tag{7}$$

These relations enable us to extrapolate the ground-state energy density in the thermodynamic limit.

A. Ground state energy scaling

To verify the scaling behavior stated in Eq. (6), we perform periodic PEPS simulations at $\lambda = \lambda_c = 3.04438$ by varying linear system size L. The results are shown in Fig. 4 for $D = 2$ and $D = 3$ PEPS bond dimensions. To speed up the convergence of our optimization, we start from system size $L = 3$; to obtain the ground state of a system with linear size L, we use an optimized PEPS tensor for a system with $(L-1) \times (L-1)$ sites as a starting point. Even though starting from a random tensor

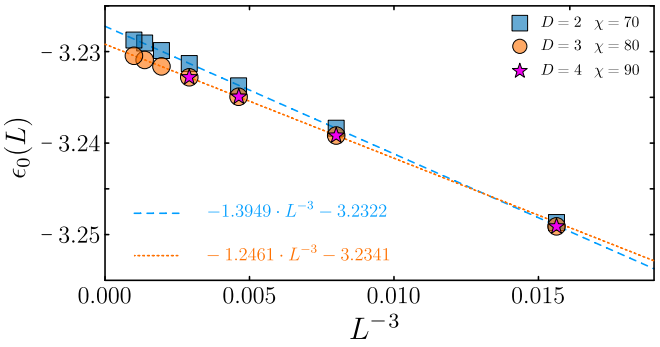

FIG. 4. Ground state energy ϵ_0 at the critical point $\lambda_c = 3.04438$ as a function of linear system size L for PEPS with local bond dimension $D = 2$ (blue squares), $D = 3$ (orange circles) and $D = 4$ (magenta stars). Linear fit to L^{-3} scaling shows $\epsilon_0(L \to \infty) \approx -3.2322$ and -3.2341 for $D = 2, 3$, respectively.

provides the same result, using results for a smaller system size improves the stability. Furthermore, it decreases the overall computation time of the algorithm until the optimization converges.

Figure 4 shows that ϵ_0 indeed scales as L^{-3} following the CFT argument presented above. A linear fit provides the following ground state energies in the thermodynamic limit:

$$\epsilon_0(L \to \infty) = \begin{cases} -3.2322, & D = 2, \\ -3.2342, & D = 3, \end{cases} \tag{8}$$

agreeing with infinite PEPS studies presented in [81, 96].

From the ground state energy scaling, we can extract a universal constant for criticality. α in Eq. (6) can be decomposed into

$$\alpha = v\alpha_c, \tag{9}$$

where v is a characteristic velocity, and α_c is a (Casimir) constant unique to each universality class. Using the value from a previous study $v \approx 3.323$ [97], we find

$$\alpha_c \approx 0.375.$$

This is consistent with previous studies using exact diagonalization $\alpha_c = 0.35(2)$ [98] and 0.39 [99].

The detailed list of ground state energies obtained as a function of the linear system size is presented in Table I. To strengthen our results, we perform the same simulations for local PEPS with bond dimension $D = 4$ and different system sizes. Table I and Fig. 4 (magenta stars) suggest that the ground state energies obtained for $D = 4$ are nearly identical to those observed in the $D = 3$ case. As the $D = 4$ simulations require significantly more time and memory while yielding similar results, in the following, we restrict the virtual bond dimension of PEPS to $D = 3$. We find that $D = 3$ sufficiently captures the proper scaling. In the last column of Table I, the results from a snake-pattern finite-size DMRG calculation with $\chi = 800$ are shown as a comparison – see Appendix D for a more detailed discussion on the DMRG simulations.

L	$D = 2$	$D = 3$	$D = 4$	DMRG
3	−3.2837	−3.2837	−3.2837	−3.2837
4	−3.2537	−3.2541	−3.2541	−3.2541
5	−3.2434	−3.2442	−3.2442	−3.2442
6	−3.2388	−3.2399	−3.2399	−3.2399
7	−3.2363	−3.2378	−3.2378	−3.2378
8	−3.2349	−3.2366		−3.2365
9	−3.2341	−3.2359		−3.2356
10	−3.2337	−3.2355		−3.2347
$L \to \infty$	−3.2322	−3.2342		

TABLE I. Ground state energies of the 2D quantum TFIM at the critical point $\lambda = 3.04438$.

B. Magnetization for finite h_z

Once we have obtained optimized PEPS tensors representing the ground state of the 2D TFIM, it is quite natural to extend our approach and calculate the magnetization per site $m_z = \langle \sigma^z \rangle$ along the z-axis. To proceed, we follow the same approach to evaluate the two-site expectation value as we did in PTMRG, only replacing the two-site Hamiltonian with a single-site σ^z operator.

Since finite-size systems do not support spontaneous symmetry breaking, m_z just trivially equals zero for all λ. Therefore, to break the $\mathbb{Z}_2$ symmetry explicitly in TFIM, we introduce a small longitudinal h_z field. As a result, the total Hamiltonian takes the following form:

$$\hat{H} = \hat{H}_{\text{TFIM}} - h_z \sum_i \hat{\sigma}_i^z, \quad h_z > 0. \tag{10}$$

By setting $h_z = 10^{-2}$ and PEPS bond dimension $D = 2$, we perform PTMRG minimization and, using optimized PEPS tensors, calculate m_z as a function of λ and compare different linear system sizes as shown in Fig. 5. As expected, for $\lambda = 0$, we obtain a symmetry-broken state when all the spins are aligned along the z-axis and magnetization per site $m_z = 1$. By increasing λ, m_z goes to zero, and the critical point appears around $\lambda \approx 3.0$.

V. EXTRACTING SCALING DIMENSION WITH FINITE-SIZE EFFECTS

Using our periodic PEPS algorithm, we can now start to extract the critical properties for a given quantum critical point. In general, we are interested in the scaling dimensions of the conformal field theory describing the low-energy physics around the critical point. These scaling dimensions appear in the correlation functions as

$$\langle \hat{\Phi}_g(0)\hat{\Phi}_g(r)\rangle \propto \frac{1}{|r|^{2\Delta_g}}, \tag{11}$$

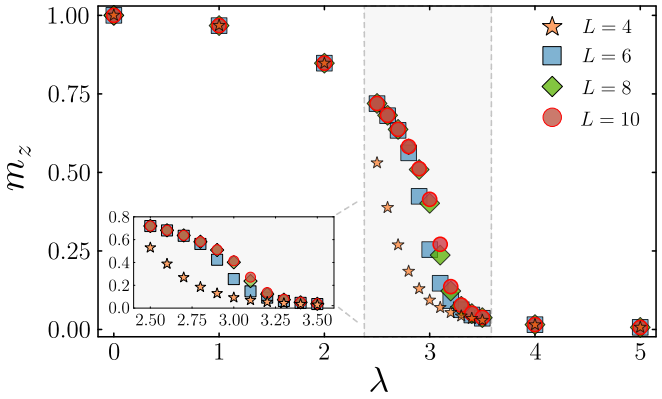

FIG. 5. The magnetization under a small uniform magnetic field with $h_z = 10^{-2}$ various system sizes $L = 4, 6, 8, 10$.

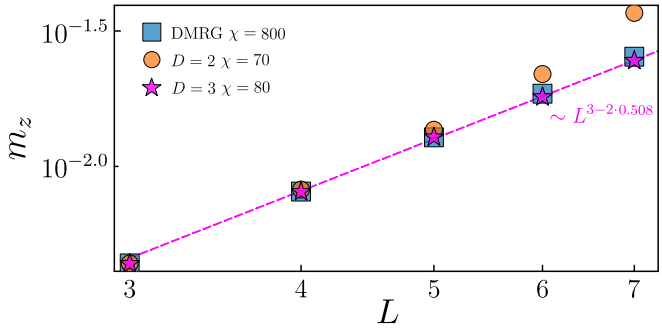

FIG. 6. Magnetization per site m_z as a function of system size L and longitudinal perturbation $h_z = 10^{-3}$ for PEPS bond dimension $D = 2$ (orange circles) and $D = 3$ (magenta stars) compared with DMRG simulation (blue squares). $\Delta_\sigma = 0.508$ is extrapolated from a polynomial fit (magenta dashed line).

where the scaling dimension is denoted as Δ_g. This comes from the transformation rules of the operator $\hat{\Phi}_g(r) \to b^{-\Delta_g}\hat{\Phi}_g(r')$ under scale transformations $r = br'$. Equation (11) is obtained when we set $b = r$ so that $\langle\hat{\Phi}_g(0)\hat{\Phi}_g(r)\rangle \propto r^{-2\Delta_g}\langle\hat{\Phi}_g(0)\hat{\Phi}_g(1)\rangle$.

Here we will extract these scaling dimensions by perturbing the critical Hamiltonian with an operator $\hat{\Phi}$, and reading off the scaling dimension from the scale dependence of the amplitude of the perturbation. In effective field theory, this can be expressed as

$$\hat{H}_{\text{pert}} = \hat{H}^*_{\text{CFT}} + \sum_n g_n \int_0^{Lx,Ly} \hat{\Phi}_n(\mathbf{r}) d^2\mathbf{r}, \tag{12}$$

where n represents all possible perturbations with corresponding $\hat{\Phi}_n(\mathbf{r})$ operators, and g_n is the running couplings. In the case of the 2D quantum TFIM, there are two relevant perturbations, $\hat{\Phi}_\epsilon(\mathbf{r})$ and $\hat{\Phi}_\sigma(\mathbf{r})$ that respectively correspond to uniform transverse ($\hat{\sigma}^x$) and longitudinal ($\hat{\sigma}^z$) perturbations from the critical coupling λ_c and 0. In the following, we neglect the contributions from the irrelevant operators as they are significantly smaller than those of relevant operators.

Let us consider the $\hat{\Phi}_\sigma(\mathbf{r})$ perturbation. In this case, the Hamiltonian takes the following form:

$$\begin{aligned}\hat{H}^\sigma_{\text{pert}} &= \hat{H}^*_{\text{CFT}} + g_\sigma \hat{V} \\ &= \hat{H}^*_{\text{CFT}} + g_\sigma \int_0^{Lx,Ly} \hat{\Phi}_\sigma(\mathbf{r}) d^2\mathbf{r}.\end{aligned}$$

Let $|\psi^0\rangle, |\psi^1\rangle, |\psi^2\rangle, ...$ and $E_0, E_1, E_2, ...$ be eigenstates and eigenvalues in ascending order of nonperturbed Hamiltonian $\hat{H}^*_{\text{CFT}}$. Then, the modified ground state of the perturbed $\hat{H}^\sigma_{\text{pert}}$ according to standard perturbation theory is

$$|\psi^0\rangle_\sigma = |\psi^0\rangle + g_\sigma \frac{\langle\psi^1|\hat{V}|\psi^0\rangle}{E_0 - E_1}|\psi^1\rangle + ..., \tag{13}$$

where we keep only linear order terms $O(g_\sigma)$. Here, the ground state $|\psi^0\rangle$ and the first excited state $|\psi^1\rangle$ are even and odd under the spin-flip symmetry. Given that the longitudinal magnetic field $\hat{V}$ is odd under the same symmetry, it allows for nonzero magnetization from the cross terms of these two states. Using this, the magnetization per site m_z becomes

$$\begin{aligned} m_z &= \langle\psi^0_\sigma|\hat{\sigma}^z|\psi^0_\sigma\rangle \\ &\simeq \langle\psi^0|\hat{\sigma}^z|\psi^1\rangle g_\sigma \left(\frac{\langle\psi^1|\hat{V}|\psi^0\rangle}{E_0 - E_1}\right) + H.c. \\ &\propto \text{Re}\left(2\langle\psi^0|\hat{\sigma}^z|\psi^1\rangle g_\sigma \frac{\langle\psi^1|\hat{V}|\psi^0\rangle}{E_0 - E_1}\right). \end{aligned} \tag{14}$$

The first term $\langle\psi^0|\hat{\sigma}^z|\psi^1\rangle$ scales as $L^{-\Delta_\sigma}$, following the scaling of the Ψ_σ operator. Similarly, the matrix element $\langle\psi^1|\hat{V}|\psi^0\rangle$ can be evaluated with the scaling relation as $\langle\psi^1|\int_0^L d^2r\hat{\Phi}_\sigma|\psi^0\rangle \propto L^{2-\Delta_\sigma}$ and $E_0 - E_1 \propto L^{-1}$ at the critical point. As a result, we get the following scaling for the magnetization per site as

$$m_z \propto L^{3-2\Delta_\sigma}. \tag{15}$$

In more generic cases, the exponents consist of the scaling of the operator and the amplitude of the perturbation/running couplings. The first one scales as $L^{-\Delta_\sigma}$, while the second $L^{d-\Delta_\sigma}$ for the systems with d space-time dimensions. The latter is nothing but the RG dimension of the operator $\hat{\Phi}_\sigma$. Similarly, we can also read out the RG dimensions of other operators by perturbing the critical Hamiltonian with the corresponding operators.

To confirm the scaling behavior in Eq. (15), we perform PTMRG optimization of periodic PEPS with bond dimensions $D = 2, 3$ at the critical point $\lambda = 3.04438$ and longitudinal perturbations $h_z = 10^{-3}$. We calculate the magnetization m_z per site for different linear system sizes L, as shown in Fig. 6. We confirm that we find a power-law behavior as a function of L and m_z for our PEPS simulations with bond dimension $D = 3$. Using

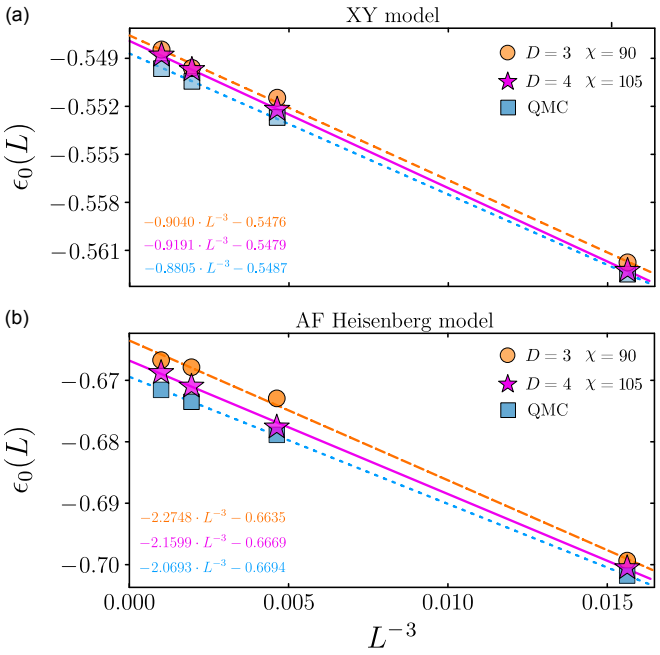

FIG. 7. Ground state energy ϵ_0 of 2D (a) XY and (b) AF Heisenberg models as a function of linear system size L for $\mathbb{Z}_2$-PEPS with local bond dimension $D = 3$ (orange circles) and $D = 4$ (magenta stars). Blue squared points show QMC results presented in (a) [102] and (b) [103]. Linear fit to L^{-3} scaling shows (a) $\epsilon_0(L \to \infty) \approx -0.5476$ and -0.5479 and (b) $\epsilon_0(L \to \infty) \approx -0.6635$ and -0.6669 for $D = 3, 4$, respectively.

Eq. (15), one can read off the scaling dimension from its power-law exponent as

$$\Delta_\sigma = 0.508, \tag{16}$$

in a reasonable agreement with the value in the literature $\Delta_\sigma = 0.518148806(24)$ and 0.524 respectively obtained from conformal bootstrap [100] and fuzzy sphere regularization [101].

VI. XY AND HEISENBERG MODELS

In this section, we consider the generalized quantum Heisenberg model on a 2D square lattice, which can be represented as:

$$\hat{H} = \sum_{\langle ij \rangle} S_i^x S_j^x + S_i^y S_j^y + \Delta S_i^z S_j^z, \tag{17}$$

where $\{S^{x,y,z}\}$ are the spin-1/2 operators. $\Delta = 0$ correspond to the XY ($O(2)$) model, while $\Delta = 1$ the antiferromagnetic Heisenberg ($O(3)$) model. In the thermodynamic limit, these models spontaneously break their continuous symmetry, creating one (two) Nambu-Goldstone bosons as gapless excitations for XY (AF Heisenberg), respectively. Since it is known that these systems are critical, we study the scaling behavior of the ground state energy ϵ_0 as a function of a linear system size L.

	XY model			AF Heisenberg model		
L	$D=3$	$D=4$	QMC	$D=3$	$D=4$	QMC
4	−0.5618	−0.5623	−0.5625	−0.6993	−0.7005	−0.7018
6	−0.5515	−0.5522	−0.5527	−0.6729	−0.6777	−0.6789
8	−0.5496	−0.5498	−0.5504	−0.6679	−0.6710	−0.6735
10	−0.5485	−0.5489	−0.5496	−0.6667	−0.6688	−0.6715
$\to\infty$	−0.5476	−0.5479	−0.5487	−0.6635	−0.6669	−0.6694

TABLE II. Ground state energies of the 2D quantum XY and AF Heisenberg models obtained by PTMRG optimization and compared to QMC results as a function of a linear system size L.

To proceed, we perform PTMRG optimization of the ground state energy for PEPS bond dimensions $D = 2, 3, 4$ and impose $\mathbb{Z}_2$-symmetry. To work with single-site unit cells, we perform a sublattice rotation as well. We observe that $D = 2$ PEPS ansatz is insufficient to capture the scaling behavior since the final optimized ground state energy remains constant as the linear system size L increases. Meanwhile, for $D = 3, 4$ the obtained ground state energies are shown in Table II together with QMC results presented in Refs. [102, 103] and extrapolation to the thermodynamic limit $L \to \infty$.

Figure 7 shows the optimized ground state energy as a function of the system size L both for the (a) XY and (b) AF Heisenberg models. As expected from 3-D CFT, the energy density scales as L^{-3} and approaches the QMC results with increasing PEPS bond dimension D. The Casimir constants for the XY and AF Heisenberg models are found to be,

$$\begin{cases} \alpha_c^{XY} \approx 0.813 & \text{for XY model,} \\ \alpha_c^{HB} \approx 1.302 & \text{for AF Heisenberg model,} \end{cases} \tag{18}$$

after substituting the corresponding spin-wave velocities $v_{XY} = 1.123$ and $v_{HB} = 1.65847$ in the literatures [102, 104]. Our estimations are in good agreement with $\alpha_{QMC}^{XY} = 0.781$ and $\alpha_{QMC}^{HB} = 1.246$ obtained from QMC simulations in [102, 103]. The list of the calculated Casimir constants is presented in Table III together with the values from previous studies. For 2-D quantum critical systems on the torus, those values can be used to detect the universality class in future studies.

VII. CONCLUSION AND OUTLOOK

In summary, we propose a novel PTMRG algorithm to contract 2-D tensor networks with periodic boundary conditions at a significantly lower computational cost compared to the well-established TRG and HOTRG schemes. By acquiring data for linearly growing system sizes, we demonstrate the performance of PTMRG for

Casimir critical constant α_c		
Model	PTMRG	previous works
Transverse-field Ising	0.375	0.35 [98]
XY	0.813	0.781 [102]
AF Heisenberg	1.302	1.246 [103]

TABLE III. Casimir critical factor α_c extracted from the ground energy scaling with linear system size for 2D QTIM, XY, and AF Heisenberg models.

problems in 2-D statistical mechanics and benchmark the universality of the transfer matrix spectrum of the 2D classical Ising model at criticality.

For 2-D quantum lattice models, we perform the variational optimization using AD-computed gradients on top of the PTMRG contraction scheme, thus obtaining a fully periodic and uniform PEPS algorithm. We demonstrate finite-size scaling of ground state energies for the 2-D transverse-field Ising model on a torus both for gapless and gapped phases. We extend the algorithm towards the extraction of scaling dimensions via finite-size effects. The torus geometry as a PEPS tensor network enables us to support our numerics with effective field theory arguments. Finally, we perform finite-size scaling of the ground state energies for XY and Heisenberg models, which are quite challenging for PEPS due to long-range order and quantum fluctuations, and demonstrate the performance of our approach as compared to state-of-the-art QMC results. By further improving the gradient computation using, e.g., a more performant AD engine and checkpointing strategies, we will likely be able to further push the quality of these results.

We believe that our findings can support ongoing research in the tensor network simulation of quantum criticality in 2+1 dimensions. In particular, the periodic finite-size approach is complementary to finite-entanglement scaling for infinite PEPS. The next step would consist of going beyond ground states and computing excitation spectra on the torus with PEPS, as torus spectroscopy can be a very powerful method for revealing the scaling dimensions of exotic phase transitions [97, 105–107]. Generalizing the excitation ansatz to the setting of periodic PEPS would be very natural, as this approach was shown to work well for infinite PEPS [108–110] as well as periodic MPS [46–48, 111].

Finally, it would be very interesting to explore boundary conditions different from the simple periodic ones we have considered here. Our scheme should be able to adopt the twisted boundary conditions phrased in terms of tube algebras and tensor networks [112, 113], which is important to probe all sectors of the theory.

ACKNOWLEDGEMENT

The authors thank Andreas Läuchli for inspiring discussions. G.F. was supported by the grant BOF23/GOA/021 from Ghent University. A.U. was supported by the MERIT-WINGS Program at the University of Tokyo, the JSPS fellowship (DC1), BOF-GOA (grant No. BOF23/GOA/021), and Watanabe Foundation. This work was supported by the Research Foundation Flanders (FWO) via grant GOE1520N, EOS (grant No. 40007526), IBOF (grant No. IBOF23/064), and BOF- GOA (grant No. BOF23/GOA/021). All the simulations were performed using the TensorKit.jl package [114].

Note added: After completion of this work, we became aware of Ref. 115, which presents a tensor renormalization scheme that is very similar to the one presented in this work, also consisting of a corner and horizontal and vertical edge tensors and a linear rather than exponential coarse-graining strategy. The specific update rules for the tensors are different, and this work further factorizes the four-leg corner tensor into two three-leg tensors, which further reduces the computational complexity to $O(\chi^4)$. This scheme was only tested on the partition function of the classical Ising model, so it would be useful to compare both schemes in the context of PEPS optimization.

Appendix A: 2D Quantum Transverse field Ising model: gapped phase

The ground state energy of gapped phases scales differently from that of critical systems as in Eq. (7) in the main text. To confirm this exponential decay of the finite-size effects, we simulate the transverse field Ising model away from the critical point $\lambda = 3.3$. The obtained ground state energy indeed converges quickly with increasing the system size, as shown in Fig. 8. As for more precise scaling, we extrapolate the ground state energy in the thermodynamic limit from the finite-size data according to Eq. (7). The result is illustrated in the insert, which confirms that the finite size correction to the ground state is exponential as $\epsilon_0(L) - \epsilon_0(\infty) \sim \frac{e^{-L/\xi}}{L^2}$. In addition, we list the numerical data with respect to the bond dimension D in Table IV. The energy is almost identical for all D, indicating that the gapped phases do not require a high bond dimension.

Appendix B: Discontinuities during gradient optimization

In the main text, we highlight the pathological issue that could appear while performing gradient-based optimization with PEPS algorithms that involve truncation. This is due to the possible discontinuity of the approximate energy evaluation as a function of the variational

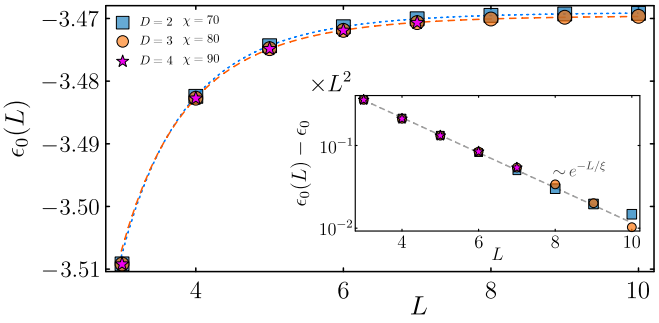

FIG. 8. Ground state energy ϵ_0 at the gapped phase $\lambda = 3.3$ as a function of linear system size L for PEPS with local bond dimension $D = 2$ (blue squares), $D = 3$ (orange circles), $D = 4$ (magenta stars). (Insert) Linear fit of the difference between extrapolated value ϵ_0 when $L \to \infty$ and $\epsilon_0(L)$ scales exponentially with the system size L.

L	$D=2$	$D=3$	$D=4$
3	−3.5092	−3.5092	−3.5092
4	−3.4824	−3.4827	−3.4827
5	−3.4743	−3.4748	−3.4748
6	−3.4713	−3.4719	−3.4719
7	−3.4700	−3.4707	−3.4707
8	−3.4695	−3.4701	
9	−3.4693	−3.4698	
10	−3.4692	−3.4697	
$L \to \infty$	−3.4690	−3.4696	

TABLE IV. Ground state energies of the 2D quantum TFIM in the paramagnetic phase at $\lambda = 3.3$.

parameters in the PEPS tensors when we employ insufficient truncation dimension, which can ultimately be traced down to level crossings in the singular value spectra on which the truncation will act. We observe that this issue arises, in particular, when studying more challenging models with larger correlation lengths. To demonstrate it, we simulate the AF Heisenberg model with the PEPS bond dimension $D = 3$ and truncation dimension $\chi = 30$. Here, the bond dimension of the double-layer PEPS tensor is $D^2 = 9$, which induces enormous truncation errors during the contraction of the tensors.

Figure 9(a) shows the obtained gradient of the energy ∇E as a function of optimization steps N_{iter}. We observe that the gradient decreases up to ≈ 25 iteration steps, but then the gradient starts increasing until the gradient optimization breaks down and can not find the direction to optimize the energy, while the gradient norm is still relatively large, taking values around 10^{-1}. To see what is causing this failure, we compute the energy landscape for this particular PEPS tensor that breaks the line search, which amounts to a one-dimensional parameter search β to find the energy minimum. Figure 9(b)

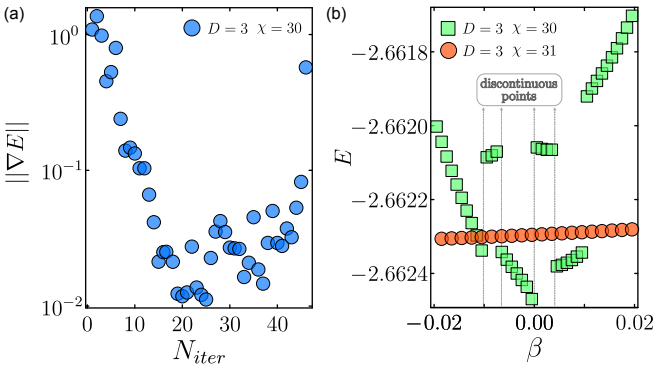

FIG. 9. An example of the discontinuity appearing in the (approximate) energy when we use an insufficient truncation dimension χ. (a) The gradient of the AF Heisenberg ground state energy as a function iteration number N_{iter}. The gradient exhibits an abrupt increase after 50 iterations. (b) The energy landscape at this unfavorable point. β is a one-dimensional parameter on the parameter space of the PEPS tensor. For $\chi = 30$, the energy is discontinuous, preventing the possibility of using gradient optimization, as the line-search will fail. This issue is fixed once you have a sufficiently large truncation dimension.

demonstrates how the energy behaves along the gradient direction $\beta \cdot \nabla E_A$ where $\beta \in [-0.02, 0.02]$. For $\chi = 30$, there are several discontinuous points where the energy E experiences sudden jumps, as denoted with gray vertical lines. These discontinuities are not representative of those of the exact energy function, which can be assumed to be a smooth function of the variational parameters, but can unfortunately not be computed efficiently. Hence, these discontinuities result from the approximation, more specifically, the truncation step, which is here based on a singular value decomposition. A level crossing of singular values around the truncation dimension will cause a sudden jump in the associated singular vectors that are kept versus discarded. These discontinuities will confuse the line search process, causing it to fail. Furthermore, with AD we obtain the exact gradient of this approximate energy landscape, and the gradient optimization can thus be guided towards directions with larger truncation errors, if these errors have the effect of lowering the energy approximation (to nonphysical values). As illustrated in Fig. 9(b), increasing the bond dimension to $\chi = 31$ resolves the discontinuities in this region of the energy landscape, but might of course cause discontinuities elsewhere. Hence, the bond dimension χ needs to be sufficiently high to avoid discontinuities altogether, or at least make them very small compared to the natural steps taken in the optimization process. Hence, a balance needs to be found between sufficient accuracy and manageable computational cost, as increasing χ, of course, affects the overall computation time and memory required, in particular in combination with the use of AD for computing the gradient via back-propagation.

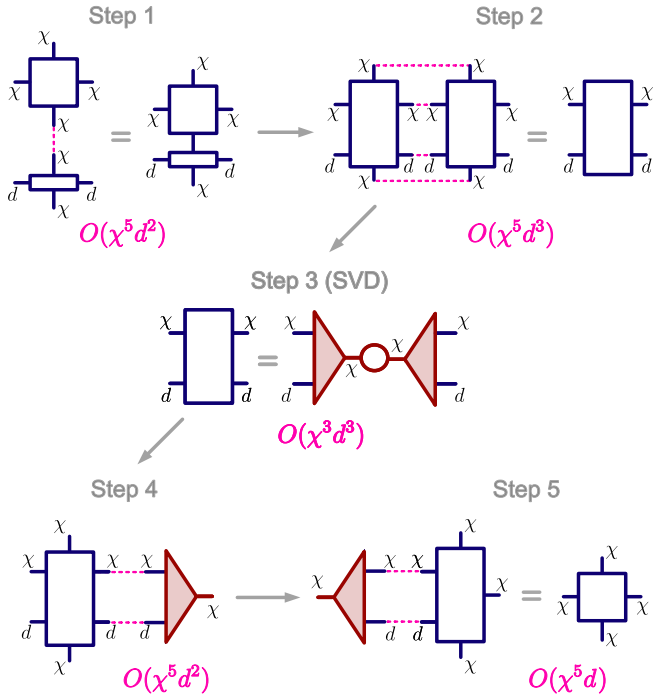

FIG. 10. An example of a single PTMRG step that updates corner tensor with computational cost per each contraction sub-step.

Appendix C: Computational cost of a single PTMRG step

One of the main findings of the manuscript is the reduction of the computational cost of a single RG step. Namely, by linearly increasing the system size, we can achieve $O(\chi^5)$ scaling instead of $O(\chi^6)$ and $O(\chi^7)$ for TRG and HOTRG, respectively. In this section, we confirm this statement by considering a single RG step to update the corner tensor as explained in the main text.

Let us consider a corner tensor with four legs (each with a bond dimension χ) and a horizontal edge tensor (top/bottom legs with bond dimension χ and left/right legs with bond dimension d). The steps within a single PTMRG step are shown in Fig. 10 and explained below:

1: Contract the corner and edge tensor along their shared leg of dimension $\chi \rightarrow$ cost $O(\chi^5 d^2)$
2: Contract the resulting tensor with its adjoint along 3 legs of dimension χ and one leg of dimension $d \rightarrow$ cost $O(\chi^5 d^3)$
3: Perform an SVD on the resulting $(\chi d) \cdot (\chi d)$ matrix $\rightarrow$ cost $O(\chi^3 d^3)$
4: Use the resulting isometry to absorb the edge tensor into the corner, by first contracting it with the tensor from Step 1 along a leg of dimension χ and one leg of dimension $d \rightarrow$ cost $O(\chi^5 d^2)$
5: Now also contract with the isometry from the other side to obtain the updated corner tensor $\rightarrow$ cost $O(\chi^5 d)$

As a result, the leading order of the computational cost with respect to the truncation dimension χ is $O(\chi^5)$. The fact that the former works with tensors that have the bond dimension d of the initial local 4-leg tensors is an intuitive explanation for why the numerical cost of PTMRG is χ^2 cheaper than that of HOTRG. Updates for edge tensors require even less cost since by definition the tensors have two legs with bond dimension χ and two legs with bond dimension d. For the non-symmetric case, we can generalize this strategy by using an "oblique projector" as described in Refs. 29, 60, 61, and 78.

Appendix D: DMRG simulation

In the main text, we present the ground state energies of the 2-D quantum transverse field Ising model (TFIM) on a square lattice at the critical point to illustrate the performance of the proposed PEPS optimisation algorithm. As no exact results are known, we also provide DMRG results for the same system. Here, we snake the MPS (with open boundary conditions) as in conventional cylinder-DMRG studies, but now also have to include the interactions between the first and last column. While we only reported the ground state energies for the largest bond dimension $\chi = 800$, here we would like to provide more details. In particular, Table V shows the ground state energies per site for $\chi = 100, 150, 200, 250, 300, 500, 800$ and system sizes $L = 3, 4, ..., 10$.

Fig. 11 shows the comparison between DMRG energies and the ones obtained from PTMRG optimization for PEPS with local bond dimension $D = 3$. One can see that while the PEPS results allow one to achieve robust scaling of the energies with the system size, the DMRG results show worse performance starting from the system size $L = 8$. A similar conclusion can be drawn from Fig. 6 in the main text, where the magnetization m_z obtained from DMRG cannot reproduce the desired scaling, while at the same time the proposed PEPS optimization provides a proper extrapolation of the scaling dimension.

[1] M. E. Fisher and M. N. Barber, Scaling theory for finite-size effects in the critical region, Phys. Rev. Lett. **28**, 1516 (1972).
[2] K. Binder, Finite size scaling analysis of Ising model

L	$\chi = 100$	$\chi = 150$	$\chi = 200$	$\chi = 250$	$\chi = 300$	$\chi = 500$	$\chi = 800$
3	−3.2837	−3.2837	−3.2837	−3.2837	−3.2837	−3.2837	−3.2837
4	−3.2541	−3.2541	−3.2541	−3.2541	−3.2541	−3.2541	−3.2541
5	−3.2441	−3.2442	−3.2442	−3.2442	−3.2442	−3.2442	−3.2442
6	−3.2396	−3.2398	−3.2399	−3.2399	−3.2399	−3.2399	−3.2399
7	−3.2368	−3.2373	−3.2375	−3.2376	−3.2377	−3.2378	−3.2378
8	−3.2345	−3.2354	−3.2359	−3.2361	−3.2363	−3.2365	−3.2365
9	−3.2323	−3.2338	−3.2344	−3.2348	−3.2351	−3.2356	−3.2356
10	−3.2305	−3.2321	−3.2330	−3.2336	−3.2340	−3.2347	−3.2347

TABLE V. Ground state energies of the 2D quantum TFIM at the critical point $\lambda = 3.04438$ obtained via periodic DMRG, χ states for the truncation bond dimension.

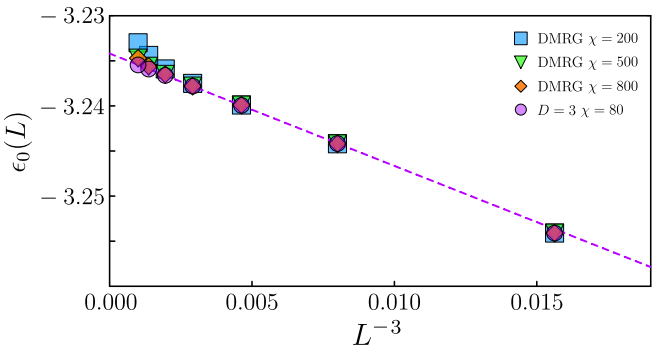

FIG. 11. Ground state energy ϵ_0 at the critical point $\lambda_c = 3.04438$ as a function of linear system size L from DMRG with truncation bond dimension $\chi = 200, 500, 800$ compared with the energies obtained from PEPS with bond dimension $D = 3$ following PTMRG approach. The dashed magenta line shows the energy scaling behavior for PEPS data points.

block distribution functions, Z. Phys. B **43**, 119 (1981).

[3] Brézin, E., An investigation of finite size scaling, J. Phys. France **43**, 15 (1982).

[4] J. L. Cardy, *Finite-size Scaling* (North-Holland, 1988).

[5] T. Xiang, *Density Matrix and Tensor Network Renormalization* (Cambridge University Press, 2023).

[6] T. Nishino, K. Okunishi, and M. Kikuchi, Numerical renormalization group at criticality, Physics Letters A **213**, 69 (1996).

[7] L. Tagliacozzo, T. R. de Oliveira, S. Iblisdir, and J. I. Latorre, Scaling of entanglement support for matrix product states, Phys. Rev. B **78**, 024410 (2008).

[8] F. Pollmann, S. Mukerjee, A. M. Turner, and J. E. Moore, Theory of finite-entanglement scaling at one-dimensional quantum critical points, Phys. Rev. Lett. **102**, 255701 (2009).

[9] B. Pirvu, G. Vidal, F. Verstraete, and L. Tagliacozzo, Matrix product states for critical spin chains: Finite-size versus finite-entanglement scaling, Phys. Rev. B **86**, 075117 (2012).

[10] U. Schollwöck, The density-matrix renormalization group in the age of matrix product states, Annals of Physics **326**, 96 (2011).

[11] M. M. Rams, P. Czarnik, and L. Cincio, Precise extrapolation of the correlation function asymptotics in uniform tensor network states with application to the bose-hubbard and xxz models, Phys. Rev. X **8**, 041033 (2018).

[12] J. C. Pillay and I. P. McCulloch, Cumulants and scaling functions of infinite matrix product states, Phys. Rev. B **100**, 235140 (2019).

[13] B. Vanhecke, J. Haegeman, K. Van Acoleyen, L. Vanderstraeten, and F. Verstraete, Scaling hypothesis for matrix product states, Phys. Rev. Lett. **123**, 250604 (2019).

[14] A. A. Eberharter, L. Vanderstraeten, F. Verstraete, and A. M. Läuchli, Extracting the speed of light from matrix product states, Phys. Rev. Lett. **131**, 226502 (2023).

[15] R.-Z. Huang, L. Zhang, A. M. Läuchli, J. Haegeman, F. Verstraete, and L. Vanderstraeten, Emergent conformal boundaries from finite-entanglement scaling in matrix product states, Phys. Rev. Lett. **132**, 086503 (2024).

[16] J. T. Schneider, A. Ueda, Y. Liu, A. M. Läuchli, M. Oshikawa, and L. Tagliacozzo, Self-congruent point in critical matrix product states: An effective field theory for finite-entanglement scaling (2024), arXiv:2411.03954 [cond-mat.stat-mech].

[17] G. Vidal, Entanglement renormalization, Phys. Rev. Lett. **99**, 220405 (2007).

[18] G. Vidal, Class of quantum many-body states that can be efficiently simulated, Phys. Rev. Lett. **101**, 110501 (2008).

[19] V. Giovannetti, S. Montangero, and R. Fazio, Quantum multiscale entanglement renormalization ansatz channels, Phys. Rev. Lett. **101**, 180503 (2008).

[20] R. N. C. Pfeifer, G. Evenbly, and G. Vidal, Entanglement renormalization, scale invariance, and quantum criticality, Phys. Rev. A **79**, 040301 (2009).

[21] M. Levin and C. P. Nave, Tensor renormalization group approach to two-dimensional classical lattice models, Phys. Rev. Lett. **99**, 120601 (2007).

[22] Z.-C. Gu, M. Levin, and X.-G. Wen, Tensor-entanglement renormalization group approach as a unified method for symmetry breaking and topological phase transitions, Phys. Rev. B **78**, 205116 (2008).

[23] Z. Y. Xie, H. C. Jiang, Q. N. Chen, Z. Y. Weng, and T. Xiang, Second renormalization of tensor-network states, Phys. Rev. Lett. **103**, 160601 (2009).

[24] Z. Y. Xie, J. Chen, M. P. Qin, J. W. Zhu, L. P.

Yang, and T. Xiang, Coarse-graining renormalization by higher-order singular value decomposition, Phys. Rev. B **86**, 045139 (2012).
[25] Y. Meurice, R. Sakai, and J. Unmuth-Yockey, Tensor lattice field theory for renormalization and quantum computing, Rev. Mod. Phys. **94**, 025005 (2022).
[26] J. F. Yu, Z. Y. Xie, Y. Meurice, Y. Liu, A. Denbleyker, H. Zou, M. P. Qin, J. Chen, and T. Xiang, Tensor renormalization group study of classical xy model on the square lattice, Phys. Rev. E **89**, 013308 (2014).
[27] G. Evenbly and G. Vidal, Tensor network renormalization, Phys. Rev. Lett. **115**, 180405 (2015).
[28] G. Evenbly, Algorithms for tensor network renormalization, Phys. Rev. B **95**, 045117 (2017).
[29] S. Yang, Z.-C. Gu, and X.-G. Wen, Loop optimization for tensor network renormalization, Phys. Rev. Lett. **118**, 110504 (2017).
[30] M. Bal, M. Mariën, J. Haegeman, and F. Verstraete, Renormalization group flows of hamiltonians using tensor networks, Phys. Rev. Lett. **118**, 250602 (2017).
[31] F. Verstraete and J. I. Cirac, Valence-bond states for quantum computation, Phys. Rev. A **70**, 060302 (2004).
[32] F. Verstraete and J. I. Cirac, Renormalization algorithms for Quantum-Many Body Systems in two and higher dimensions, arXiv 10.48550/arXiv.cond-mat/0407066 (2004), cond-mat/0407066.
[33] Y.-Y. Shi, L.-M. Duan, and G. Vidal, Classical simulation of quantum many-body systems with a tree tensor network, Phys. Rev. A **74**, 022320 (2006).
[34] L. Tagliacozzo, G. Evenbly, and G. Vidal, Simulation of two-dimensional quantum systems using a tree tensor network that exploits the entropic area law, Phys. Rev. B **80**, 235127 (2009).
[35] V. Murg, F. Verstraete, O. Legeza, and R. M. Noack, Simulating strongly correlated quantum systems with tree tensor networks, Phys. Rev. B **82**, 205105 (2010).
[36] J. Jordan, R. Orús, G. Vidal, F. Verstraete, and J. I. Cirac, Classical Simulation of Infinite-Size Quantum Lattice Systems in Two Spatial Dimensions, Phys. Rev. Lett. **101**, 250602 (2008).
[37] M. Rader and A. M. Läuchli, Finite correlation length scaling in lorentz-invariant gapless ipeps wave functions, Phys. Rev. X **8**, 031030 (2018).
[38] P. Corboz, P. Czarnik, G. Kapteijns, and L. Tagliacozzo, Finite correlation length scaling with infinite projected entangled-pair states, Phys. Rev. X **8**, 031031 (2018).
[39] B. Vanhecke, J. Hasik, F. Verstraete, and L. Vanderstraeten, Scaling hypothesis for projected entangled-pair states, Phys. Rev. Lett. **129**, 200601 (2022).
[40] Q. Mortier, M.-H. Li, J. Haegeman, and N. Bultinck, Finite-entanglement scaling of 2d metals, Phys. Rev. Lett. **131**, 266202 (2023).
[41] D. Porras, F. Verstraete, and J. I. Cirac, Renormalization algorithm for the calculation of spectra of interacting quantum systems, Phys. Rev. B **73**, 014410 (2006).
[42] P. Pippan, S. R. White, and H. G. Evertz, Efficient matrix-product state method for periodic boundary conditions, Phys. Rev. B **81**, 081103 (2010).
[43] D. Rossini, V. Giovannetti, and R. Fazio, Stiffness in 1d matrix product states with periodic boundary conditions, Journal of Statistical Mechanics: Theory and Experiment **2011**, P05021 (2011).
[44] B. Pirvu, F. Verstraete, and G. Vidal, Exploiting translational invariance in matrix product state simulations of spin chains with periodic boundary conditions, Phys. Rev. B **83**, 125104 (2011).
[45] D. Draxler, J. Haegeman, F. Verstraete, and M. Rizzi, Continuous matrix product states with periodic boundary conditions and an application to atomtronics, Phys. Rev. B **95**, 045145 (2017).
[46] Y. Zou, A. Milsted, and G. Vidal, Conformal data and renormalization group flow in critical quantum spin chains using periodic uniform matrix product states, Phys. Rev. Lett. **121**, 230402 (2018).
[47] Y. Zou, A. Milsted, and G. Vidal, Conformal fields and operator product expansion in critical quantum spin chains, Phys. Rev. Lett. **124**, 040604 (2020).
[48] Y. Zou and G. Vidal, Emergence of conformal symmetry in quantum spin chains: Antiperiodic boundary conditions and supersymmetry, Phys. Rev. B **101**, 045132 (2020).
[49] Y. Zou, K. Siva, T. Soejima, R. S. K. Mong, and M. P. Zaletel, Universal tripartite entanglement in one-dimensional many-body systems, Phys. Rev. Lett. **126**, 120501 (2021).
[50] M. Van Damme, R. Vanhove, J. Haegeman, F. Verstraete, and L. Vanderstraeten, Efficient matrix product state methods for extracting spectral information on rings and cylinders, Phys. Rev. B **104**, 115142 (2021).
[51] S. Dong, C. Wang, H. Zhang, M. Zhang, and L. He, (2024), arXiv:2407.15333 [cond-mat.str-el].
[52] R. J. Baxter, Dimers on a Rectangular Lattice, Journal of Mathematical Physics **9**, 650 (1968).
[53] R. J. Baxter, Variational approximations for square lattice models in statistical mechanics, Journal of Statistical Physics **19**, 461 (1978).
[54] T. Nishino and K. Okunishi, Corner transfer matrix renormalization group method, Journal of the Physical Society of Japan **65**, 891 (1996).
[55] T. Nishino and K. Okunishi, Corner transfer matrix algorithm for classical renormalization group, Journal of the Physical Society of Japan **66**, 3040–3047 (1997).
[56] M. T. Fishman, L. Vanderstraeten, V. Zauner-Stauber, J. Haegeman, and F. Verstraete, Faster methods for contracting infinite two-dimensional tensor networks, Phys. Rev. B **98**, 235148 (2018).
[57] L. Vanderstraeten, L. Burgelman, B. Ponsioen, M. Van Damme, B. Vanhecke, P. Corboz, J. Haegeman, and F. Verstraete, Variational methods for contracting projected entangled-pair states, Phys. Rev. B **105**, 195140 (2022).
[58] R. Orús and G. Vidal, Simulation of two-dimensional quantum systems on an infinite lattice revisited: Corner transfer matrix for tensor contraction, Phys. Rev. B **80**, 094403 (2009).
[59] P. Corboz, J. Jordan, and G. Vidal, Simulation of fermionic lattice models in two dimensions with projected entangled-pair states: Next-nearest neighbor hamiltonians, Phys. Rev. B **82**, 245119 (2010).
[60] P. Corboz, T. M. Rice, and M. Troyer, Competing states in the t-j model: Uniform d-wave state versus stripe state, Phys. Rev. Lett. **113**, 046402 (2014).
[61] S. Iino, S. Morita, and N. Kawashima, Boundary tensor renormalization group, Phys. Rev. B **100**, 035449 (2019).
[62] D. Adachi, T. Okubo, and S. Todo, Anisotropic tensor renormalization group, Phys. Rev. B **102**, 054432 (2020).

[63] D. Adachi, T. Okubo, and S. Todo, Bond-weighted tensor renormalization group, Phys. Rev. B **105**, L060402 (2022).

[64] D. Kadoh and K. Nakayama, (2019), arXiv:1912.02414 [hep-lat].

[65] S. Akiyama, Y. Meurice, and R. Sakai, Tensor renormalization group for fermions, J. Phys. Condens. Matter **36**, 343002 (2024), arXiv:2401.08542 [hep-lat].

[66] M. Bal, M. Mariën, J. Haegeman, and F. Verstraete, Renormalization group flows of hamiltonians using tensor networks, Phys. Rev. Lett. **118**, 250602 (2017).

[67] M. Hauru, C. Delcamp, and S. Mizera, Renormalization of tensor networks using graph-independent local truncations, Phys. Rev. B **97**, 045111 (2018).

[68] K. Homma, T. Okubo, and N. Kawashima, Nuclear norm regularized loop optimization for tensor network, Phys. Rev. Res. **6**, 043102 (2024).

[69] L. De Lathauwer, B. De Moor, and J. Vandewalle, A Multilinear Singular Value Decomposition, SIAM J. Matrix Anal. Appl. (2006).

[70] Y. Liu, Y. Meurice, M. P. Qin, J. Unmuth-Yockey, T. Xiang, Z. Y. Xie, J. F. Yu, and H. Zou, Exact blocking formulas for spin and gauge models, Phys. Rev. D **88**, 056005 (2013).

[71] A. Ueda and M. Oshikawa, Resolving the berezinskii-kosterlitz-thouless transition in the two-dimensional xy model with tensor-network-based level spectroscopy, Phys. Rev. B **104**, 165132 (2021).

[72] A. Ueda and M. Oshikawa, Finite-size and finite bond dimension effects of tensor network renormalization, Phys. Rev. B **108**, 024413 (2023).

[73] C.-Y. Huang, S.-H. Chan, Y.-J. Kao, and P. Chen, Tensor network based finite-size scaling for two-dimensional ising model, Phys. Rev. B **107**, 205123 (2023).

[74] J. L. Cardy, Conformal invariance and universality in finite-size scaling, J. Phys. A **17**, L385 (1984).

[75] J. L. Cardy, Operator Content of Two-Dimensional Conformally Invariant Theories, Nucl. Phys. B **270**, 186 (1986).

[76] Z.-C. Gu and X.-G. Wen, Tensor-entanglement-filtering renormalization approach and symmetry-protected topological order, Phys. Rev. B **80**, 155131 (2009).

[77] H. C. Jiang, Z. Y. Weng, and T. Xiang, Accurate Determination of Tensor Network State of Quantum Lattice Models in Two Dimensions, Phys. Rev. Lett. **101**, 090603 (2008).

[78] L. Wang and F. Verstraete, Cluster update for tensor network states (2011), arXiv:1110.4362 [cond-mat.str-el].

[79] H. N. Phien, J. A. Bengua, H. D. Tuan, P. Corboz, and R. Orús, Infinite projected entangled pair states algorithm improved: Fast full update and gauge fixing, Phys. Rev. B **92**, 035142 (2015).

[80] P. Corboz, Variational optimization with infinite projected entangled-pair states, Phys. Rev. B **94**, 035133 (2016).

[81] L. Vanderstraeten, J. Haegeman, P. Corboz, and F. Verstraete, Gradient methods for variational optimization of projected entangled-pair states, Phys. Rev. B **94**, 155123 (2016).

[82] A. G. Baydin, B. A. Pearlmutter, A. A. Radul, and J. M. Siskind, Automatic differentiation in machine learning: a survey, Journal of Marchine Learning Research **18**, 1 (2018).

[83] H.-J. Liao, J.-G. Liu, L. Wang, and T. Xiang, Differentiable programming tensor networks, Phys. Rev. X **9**, 031041 (2019).

[84] M. Lubasch, J. I. Cirac, and M.-C. Bañuls, Algorithms for finite projected entangled pair states, Phys. Rev. B **90**, 064425 (2014).

[85] M. Scheb and R. M. Noack, Finite projected entangled pair states for the hubbard model, Phys. Rev. B **107**, 165112 (2023).

[86] W.-Y. Liu, S.-J. Dong, Y.-J. Han, G.-C. Guo, and L. He, Gradient optimization of finite projected entangled pair states, Phys. Rev. B **95**, 195154 (2017).

[87] T. Vieijra, J. Haegeman, F. Verstraete, and L. Vanderstraeten, Direct sampling of projected entangled-pair states, Phys. Rev. B **104**, 235141 (2021).

[88] M. P. Zaletel and F. Pollmann, Isometric tensor network states in two dimensions, Phys. Rev. Lett. **124**, 037201 (2020).

[89] S.-H. Lin, M. P. Zaletel, and F. Pollmann, Efficient simulation of dynamics in two-dimensional quantum spin systems with isometric tensor networks, Phys. Rev. B **106**, 245102 (2022).

[90] R. H. Byrd, P. Lu, J. Nocedal, and C. Zhu, A Limited Memory Algorithm for Bound Constrained Optimization, SIAM J. Sci. Comput. (2006).

[91] V. Privman and M. E. Fisher, Universal critical amplitudes in finite-size scaling, Phys. Rev. B **30**, 322 (1984).

[92] A. Klumper and M. T. Batchelor, An analytic treatment of finite-size corrections in the spin-1 antiferromagnetic XXZ chain, J. Phys. A: Math. Gen. **23**, L189 (1990).

[93] P. A. Pearce and A. Klümper, Finite-size corrections and scaling dimensions of solvable lattice models: An analytic method, Phys. Rev. Lett. **66**, 974 (1991).

[94] C. Destri and H. J. de Vega, Unified approach to Thermodynamic Bethe Ansatz and finite size corrections for lattice models and field theories, Nucl. Phys. B **438**, 413 (1995).

[95] M. Dugave, F. Göhmann, K. K. Kozlowski, and J. Suzuki, On form-factor expansions for the XXZ chain in the massive regime, J. Stat. Mech.: Theory Exp. **2015** (5), P05037.

[96] M. Rader and A. M. Läuchli, Finite Correlation Length Scaling in Lorentz-Invariant Gapless iPEPS Wave Functions, Phys. Rev. X **8**, 031030 (2018).

[97] M. Schuler, S. Whitsitt, L.-P. Henry, S. Sachdev, and A. M. Läuchli, Universal signatures of quantum critical points from finite-size torus spectra: A window into the operator content of higher-dimensional conformal field theories, Phys. Rev. Lett. **117**, 210401 (2016).

[98] C. J. Hamer, Finite-size scaling in the transverse ising model on a square lattice, Journal of Physics A: Mathematical and General **33**, 6683–6698 (2000).

[99] M. Henkel and A. Patkos, Conformal invariance and line defects in the two-dimensional ising model, Journal of Physics A: Mathematical and General **21**, L231 (1988).

[100] C.-H. Chang, V. Dommes, R. S. Erramilli, A. Homrich, P. Kravchuk, A. Liu, M. S. Mitchell, D. Poland, and D. Simmons-Duffin, Bootstrapping the 3d ising stress tensor, arXiv preprint arXiv:2411.15300 (2024).

[101] W. Zhu, C. Han, E. Huffman, J. S. Hofmann, and Y.-C. He, Uncovering Conformal Symmetry in the 3D Ising Transition: State-Operator Correspondence from a Quantum Fuzzy Sphere Regularization, Phys. Rev. X **13**, 021009 (2023), arXiv:2210.13482 [cond-mat.stat-

mech].
[102] A. W. Sandvik and C. J. Hamer, Ground-state parameters, finite-size scaling, and low-temperature properties of the two-dimensional $S = \frac{1}{2}$ XY model, Phys. Rev. B **60**, 6588 (1999).
[103] A. W. Sandvik, Finite-size scaling of the ground-state parameters of the two-dimensional Heisenberg model, Phys. Rev. B **56**, 11678 (1997).
[104] A. Sen, H. Suwa, and A. W. Sandvik, Velocity of excitations in ordered, disordered, and critical antiferromagnets, Phys. Rev. B **92**, 195145 (2015).
[105] S. Whitsitt, M. Schuler, L.-P. Henry, A. M. Läuchli, and S. Sachdev, Spectrum of the wilson-fisher conformal field theory on the torus, Phys. Rev. B **96**, 035142 (2017).
[106] M. Schuler, S. Hesselmann, S. Whitsitt, T. C. Lang, S. Wessel, and A. M. Läuchli, Torus spectroscopy of the gross-neveu-yukawa quantum field theory: Free dirac versus chiral ising fixed point, Phys. Rev. B **103**, 125128 (2021).
[107] A. Wietek, S. Capponi, and A. M. Läuchli, Quantum electrodynamics in $2 + 1$ dimensions as the organizing principle of a triangular lattice antiferromagnet, Phys. Rev. X **14**, 021010 (2024).
[108] L. Vanderstraeten, M. Mariën, F. Verstraete, and J. Haegeman, Excitations and the tangent space of projected entangled-pair states, Phys. Rev. B **92**, 201111 (2015).
[109] L. Vanderstraeten, J. Haegeman, and F. Verstraete, Simulating excitation spectra with projected entangled-pair states, Phys. Rev. B **99**, 165121 (2019).
[110] B. Ponsioen and P. Corboz, Excitations with projected entangled pair states using the corner transfer matrix method, Phys. Rev. B **101**, 195109 (2020).
[111] B. Pirvu, J. Haegeman, and F. Verstraete, Matrix product state based algorithm for determining dispersion relations of quantum spin chains with periodic boundary conditions, Phys. Rev. B **85**, 035130 (2012).
[112] N. Bultinck, M. Mariën, D. Williamson, M. Şahinoğlu, J. Haegeman, and F. Verstraete, Anyons and matrix product operator algebras, Annals of Physics **378**, 183 (2017).
[113] L. Lootens, C. Delcamp, and F. Verstraete, Dualities in one-dimensional quantum lattice models: Topological sectors, PRX Quantum **5**, 010338 (2024).
[114] J. Haegeman, Tensorkit julia package, `https://github.com/Jutho/TensorKit.jl` (2021).
[115] W. Lan and G. Evenbly, Tensor renormalization group centered about a core tensor, Physical Review B **100**, 10.1103/physrevb.100.235118 (2019).